Journal of Scientific Computing (2023) 96:83
https://doi.org/10.1007/s10915-023-02301-7

Hybrid HWENO Method for Nonlinear Degenerate Parabolic Equations

Muyassar Ahmat[1] · **Jianxian Qiu**[2]

Received: 20 March 2022 / Revised: 11 July 2023 / Accepted: 12 July 2023

Abstract
In this paper, a hybrid Hermite weighted essentially non-oscillatory scheme is proposed for nonlinear degenerate parabolic equations which may contain discontinuity in the solution. The present scheme is constructed by applying the hybrid HWENO method based on the zero- and first-order moment with DDG flux to discrete the diffusion term in spatial direction and the third-order TVD Runge–Kutta method in temporal direction. A troubled-cell indicator is first used to identify the cells in which the discontinuity may exist, then the first-order moment in the troubled-cell is reconstructed by fifth-order HWENO scheme. To avoid spurious oscillation, the HWENO reconstruction is performed when the reconstruction stencils contain troubled-cell, otherwise linear reconstruction is performed straightforwardly. Compared with WENO schemes, the present scheme has advantages: (1) compactness, only immediate neighbor cells are used in the reconstruction procedure; (2) accuracy, the numerical errors by the present scheme are smaller than those by WENO schemes. Some benchmarks for one- and two-dimensional parabolic equations to demonstrate the high order accuracy and non-oscillatory performance of the present scheme.

Keywords HWENO scheme · DDG flux · Troubled-cell indicator · Nonlinear degenerate parabolic equation · TVD Runge–Kutta method

Mathematics Subject Classification 65M60 · 35L65

The research of the first author is partially supported by Xinjiang Tianchi Talents Foundation of China under Grant 51052300533. The research of the second author is partially supported by NSFC Grant 12071392.

✉ Jianxian Qiu
jxqiu@xmu.edu.cn

Muyassar Ahmat
muyassar@xju.edu.cn

1 College of Mathematics and Systems Science, Xinjiang University, Urumqi 830017, Xinjiang, People's Republic of China

2 School of Mathematical Sciences and Fujian Provincial Key Laboratory of Mathematical Modeling and High-Performance Scientific Computing, Xiamen University, Xiamen 361005, Fujian, People's Republic of China

Published online: 02 August 2023

1 Introduction

Weighted essentially non-oscillatory (WENO) scheme is an effective method to solve the hyperbolic conservation law which the solution may contain discontinuity. After the first introduction of the third-order accurate finite volume WENO scheme [31] in one spatial dimension, a general construction for arbitrary order accurate finite difference WENO scheme was provided by Jiang and Shu [23] in 1996. A large variety of highly effective conservative finite volume and finite difference WENO schemes were widely studied since then by researchers [8, 11, 14, 20, 22, 28, 42, 52] for the hyperbolic conservation laws.

The idea of the Hermite WENO (HWENO) scheme is similar to the WENO scheme but has the advantage of keeping the compactness of the scheme by only using the immediate neighbor cell informations of the solution and its derivative for reconstruction. The WENO scheme, on the other hand, requires a wide range of cell information to achieve the same high order accuracy. Therefore, HWENO scheme achieves higher order computational accuracy than WENO scheme with the same stencil. Qiu and Shu [36, 38] presented the Hermite WENO (HWENO) methodology, which discretizes the original and derivative equation in the spatial direction. After this, various types of HWENO schemes were presented in [13, 30, 44, 47, 49, 51] for conservation law and relative equations, respectively.

Since the last decade, researchers have pay their attention to solve the nonlinear degenerate parabolic equations which may generate discontinuity in the solution by WENO method [32]. A new finite difference WENO procedure was given by using optimum polynomial in the stencil in [2]. Both explicit and implicit finite volume WENO schemes were developed on non-uniform computational meshes in [5]. An efficient sixth-order finite difference WENO scheme was obtained with a new type of nonlinear weight by Rathan [40]. High order finite difference multi-resolution WENO method for the second derivative was constructed in [24]. Abedian [1] presented a finite difference WENO scheme that can take any artificial positive linear weights(the sum equals one) by using the convex combination of two linear and one fourth degree Legendre orthogonal monic polynomials. The authors [3] also introduced a new sixth-order finite difference WENO based on exponential polynomials, the scheme can achieve the maximal approximation order in smooth regions while maintaining its accuracy in critical points.

In this paper, we design a hybrid HWENO scheme for nonlinear degenerate parabolic equation which may cause possible discontinuity. Since the smooth solution accounts for most of the probability, there is no need to use HWENO reconstruction for all cells but only the cells where the discontinuity exists. Therefore, the hybrid HWENO method is a suitable choice to achieve high-order accuracy and avoid unnecessary computation at the same time. The main purpose of the hybrid HWENO scheme is to use the linear approximation directly in the smooth regions and switch automatically to the HWENO procedure nearby discontinuity.

The switching principle is also a well-studied area in conservation laws. Various shock detecting principles were studied and compared [37] by Qiu and Shu for Runge–Kutta discontinuous Galerkin method, such as TVB [16], BDF [25], BSB [12], MP [43], MMP [41], KXRCF [27] troubled-cell indicators. Here, we use another new type of troubled-cell indicator [50], which is more simpler and effective for the present problem.

For the numerical flux of the diffusion term, we apply the direct discontinuous Galerkin (DDG) flux [29] based on the direct weak formulation for solutions of parabolic equations, which is consistent and conservative and also can ensure the nonlinear stability. Similar to the numerical flux for the convection term, DDG flux also can provide the possibility that cells communicate through numerical fluxes at cell boundaries only.

Our main focus in this paper is to capture the discontinuity caused by nonlinear degenerate parabolic equation without oscillation. Such type of equations have wide applications in collisional transport models in plasmas [17], radiative transport [26, 35], the flow of gas in a porous medium [7, 33, 46]. This type of equations, such as the porous medium equation (PME) may not have classical solution, even for the smooth initial data. Consequently, weak solutions, their existence and uniqueness are studied in [4, 34, 45]. On the other hand, various numerical schemes are attempted to solve these equations numerically such as kinetic scheme [6], relaxation scheme [15], WENO schemes [2, 5, 19, 24, 32, 40], finite volume method [10], adaptive multi-resolution scheme [9], mixed finite element method [39] and local discontinuous Galerkin finite element method [48].

Since the nonlinear degenerate parabolic equation may acts hyperbolically, it is essential to construct a numerical scheme capable of simulating these features. Therefore, it is reasonable to construct the numerical techniques, such as the HWENO technique, for solving nonlinear degenerate parabolic equation. The organization of this paper is as follows: In Sect. 2, we describe the HWENO scheme [49] with DDG flux for one- and two-dimensional parabolic equation. In Sect. 3, the numerical method in the temporal direction and stability analysis for linear equation are briefly given. The high order computational accuracy and non-oscillatory property of the hybrid HWENO scheme are provided by numerical tests in Sect. 4. Brief Conclusion is given in Sect. 5.

2 Finite Volume Hybrid HWENO Scheme

We consider the general form of advection-diffusion equation:

$$\begin{cases} u_t + \nabla \cdot F(u) = \Delta G(u), \quad x \in \mathbb{R}, t \in [t_0, T] \\ u(x, 0) = u_0(x), \quad x \in \mathbb{R}. \end{cases} \tag{2.1}$$

We first multiply the governing equation (2.1) by test function $\varphi(\mathbf{x})$, then integrate by parts over target cell $\square_0$, we can obtain the integral form as follows:

$$\begin{aligned} \frac{d}{dt}\Big[\int_{\square_0} u\varphi(\mathbf{x})d\mathbf{x}\Big] = &-\int_{\partial\square_0} \big(F(u)\cdot\mathbf{n}\big)\varphi(\mathbf{x})ds + \int_{\square_0} F(u)\cdot\nabla\varphi(\mathbf{x})d\mathbf{x} \\ &+\int_{\partial\square_0} \big(\nabla G(u)\cdot\mathbf{n}\big)\varphi(\mathbf{x})ds - \int_{\square_0} \nabla G(u)\cdot\nabla\varphi(\mathbf{x})d\mathbf{x}, \end{aligned} \tag{2.2}$$

where $\mathbf{n}$ is the outward unit normal vector to $\partial\square_0$. For the one dimensional case, the cell $\square_0$ is an interval $I_i = [x_{i-\frac{1}{2}}, x_{i+\frac{1}{2}}]$, $\varphi(\mathbf{x}) = \{\frac{1}{\Delta x}, \frac{x-x_i}{\Delta x^2}\}$. $\bar{u}_i = \int_{I_i} \frac{u}{\Delta x} dx$, $\bar{v}_i = \int_{I_i} u\frac{x-x_i}{\Delta x^2} dx$ are the zero-order moment (cell average) and first-order moment in cell I_i, respectively. For the two dimensional case, the cell $\square_0$ is a rectangle $I_{i,j} = [x_{i-\frac{1}{2}}, x_{i+\frac{1}{2}}] \times [y_{j-\frac{1}{2}}, y_{j+\frac{1}{2}}]$, $\varphi(\mathbf{x}) = \{\frac{1}{\Delta x\Delta y}, \frac{x-x_i}{\Delta x^2\Delta y}, \frac{y-y_j}{\Delta x\Delta y^2}\}$. $\bar{u}_{i,j} = \int_{I_{i,j}} \frac{u}{\Delta x\Delta y} dxdy$, $\bar{v}_{i,j} = \int_{I_{i,j}} u\frac{x-x_i}{\Delta x^2\Delta y} dxdy$, $\bar{w}_{i,j} = \int_{I_{i,j}} u\frac{y-y_j}{\Delta x\Delta y^2} dxdy$ are the zero-order moment (cell average), first-order moment in x and y direction in cell $I_{i,j}$, respectively. Δx, Δy are the spatial step size in x and y direction, respectively.

The line integrals in (2.2) are approximated by K-point Gaussian quadrature formula on the each edge of the cell, such as:

$$\begin{aligned}\int_{\partial\square_0}\big(F(u)\cdot\mathbf{n}\big)\varphi(\mathbf{x})ds &\approx \sum_{l=1}^{ll}|\partial\square_{0_l}|\sum_{k=1}^{K}\omega_k\big(F\big(u(P_{lk},t)\big)\cdot\mathbf{n}_l\big)\varphi(P_{lk}),\\ \int_{\partial\square_0}\big(\nabla G(u)\cdot\mathbf{n}\big)\varphi(\mathbf{x})ds &\approx \sum_{l=1}^{ll}|\partial\square_{0_l}|\sum_{k=1}^{K}\omega_k\big(\nabla G\big(u(P_{lk},t)\big)\cdot\mathbf{n}_l\big)\varphi(P_{lk}).\end{aligned}\tag{2.3}$$

where $\partial\square_0=\cup_{l=1}^{ll}\partial\square_{0_l}$. P_{lk} is the Gauss quadrature point on the edge $\partial\square_{0_l}$ while ω_{lk} is the corresponding normalized weight, and volume integrals in (2.2) are approximated by $K\times K-$point Gaussian quadrature formula:

$$\begin{aligned}\int_{\square_0}F(u)\cdot\nabla\varphi(\mathbf{x})d\mathbf{x} &\approx |\square_0|\sum_{l=1}^{K}\sum_{k=1}^{K}\omega_l\omega_k F\big(u(P_{lk},t)\big)\cdot\nabla\varphi(P_{lk}),\\ \int_{\square_0}\nabla G(u)\cdot\nabla\varphi(\mathbf{x})d\mathbf{x} &\approx |\square_0|\sum_{l=1}^{K}\sum_{k=1}^{K}\omega_l\omega_k\nabla G\big(u(P_{lk},t)\big)\cdot\nabla\varphi(P_{lk}).\end{aligned}\tag{2.4}$$

The flux $F\big(u(P_{lk},t)\big)\cdot\mathbf{n}_l$ and $\nabla G\big(u(P_{lk},t)\big)\cdot\mathbf{n}_l$ should be reformulated by numerical fluxes on the edge of the cell. In this paper, we choose to approximate $F\big(u(P_{lk},t)\big)\cdot\mathbf{n}_l$ by the local Lax-Friedrichs flux as follows:

$$\begin{aligned}F\big(u(P_{lk},t)\big)\cdot\mathbf{n}_l \approx{}& \frac{1}{2}\Big(F\big(u^+(P_{lk},t)\big)+F\big(u^-(P_{lk},t)\big)\Big)\cdot\mathbf{n}_l\\ &-\frac{\alpha}{2}\big(u^+(P_{lk},t)-u^-(P_{lk},t)\big),\end{aligned}\tag{2.5}$$

where α is defined as the upper bound for the eigenvalues of the Jacobian in the $\mathbf{n}_l$ direction. $u^-(P_{lk},t)$ and $u^+(P_{lk},t)$ are high order approximations to $u(P_{lk},t)$ from inside and outside of target cell $\square_0$, respectively.

The flux $\nabla G\big(u(P_{lk},t)\big)\cdot\mathbf{n}_l$ is specified by DDG flux [29]. The readers can find more detailed information about DDG flux for different choice of coefficient in [29]. Here we use this flux in the following notation:

$$\nabla G\big(u(P_{lk},t)\big)\cdot\mathbf{n}_l \approx b_0\frac{[G\big(u(P_{lk},t)\big)]}{|\partial\square_{0_l}|}\cdot\mathbf{n}_l+\overline{\nabla G\big(u(P_{lk},t)\big)}\cdot\mathbf{n}_l,\tag{2.6}$$

where $[u]=u^+-u^-$, $\bar{u}=\frac{u^++u^-}{2}$. As is tested in numerical experiment, the sum of these two terms is sufficient enough to ensure the nonlinear stability with suitable coefficient b_0 and we could have locally admissible underlying flux in each cell. In order to get the numerical fluxes in (2.5) and (2.6), we have to reconstruct $u^{\pm}(P_{lk},t)$ and $\nabla u^{\pm}(P_{lk},t)$. Now, we describe the spatial reconstruction description in following steps.

Step 1. Identify the troubled-cell and modify the first-order moment in the troubled-cell.

It is possible that $\nabla G(u)=0$ for some value of u, which leads to lose the parabolicity of the system and exhibit hyperbolic behavior, then discontinuity may appear for the solution of equation. If the solution in the target cell $\square_0$ is discontinuous, then cell $\square_0$ is marked as troubled-cell.

For one dimensional case, we use the troubled-cell indicator $\mathcal{I}(\bar{u}_{i-1}, \bar{u}_i, \bar{u}_{i+1}, \bar{v}_i)$ presented in [50] to identify the discontinuity:

$$\mathcal{I}(\bar{u}_{i-1}, \bar{u}_i, \bar{u}_{i+1}, \bar{v}_i) = \begin{cases} 1, & \tau > c_1 \Delta x^{c_2} \max\{\beta_1, \beta_2, \beta_3\}, \\ 0, & \text{Otherwise.} \end{cases} \tag{2.7}$$

when $\mathcal{I} = 1$, the cell I_i would be marked as troubled-cell. In (2.7), the $\beta_1, \beta_2, \beta_3$ and τ are defined as:

$$\begin{aligned} &\beta_1 = 144\bar{v}_i^2, \quad \beta_2 = (\bar{u}_i - \bar{u}_{i-1})^2, \quad \beta_3 = (\bar{u}_{i+1} - \bar{u}_i)^2, \\ &\tau = \left(\frac{|\beta_1 - \beta_2| + |\beta_1 - \beta_3|}{2} \right)^2, \end{aligned} \tag{2.8}$$

and two parameters c_1 and c_2 determine the sensitivity of the indicator. We tested different choices of c_1 and c_2 for the test cases in this paper under different meshes and found that $c_1 = 2$ and $c_2 = 2$ is the most reliable and more suitable choice for our problem at hand.

When the cell I_i is marked as troubled-cell, the first-order moment $\bar{v}_i$ is modified as:

$$\begin{aligned} \bar{v}_i = &\omega_0 \Big(\frac{1}{r_0} \int_{I_i} q_0(x) \frac{x - x_i}{\Delta x^2} dx - \frac{r_1}{r_0} \int_{I_i} q_1(x) \frac{x - x_i}{\Delta x^2} dx - \frac{r_2}{r_0} \int_{I_i} q_2(x) \frac{x - x_i}{\Delta x^2} dx \Big) \\ &+ \omega_1 \int_{I_i} q_1(x) \frac{x - x_i}{\Delta x^2} dx + \omega_2 \int_{I_i} q_2(x) \frac{x - x_i}{\Delta x^2} dx, \end{aligned} \tag{2.9}$$

where the linear weights r_0, r_1, r_2 can be any positive numbers with condition $r_0 + r_1 + r_2 = 1$. Polynomials $q_0(x), q_1(x), q_2(x)$ are defined as:

$$\begin{aligned} &\int_{I_{i+j}} \frac{q_0(x)}{\Delta x} dx = \bar{u}_{i+j}, \quad j = -1, 0, 1, \qquad \int_{I_{i+j}} q_0(x) \frac{(x - x_{i+j})}{\Delta x^2} dx = \bar{v}_{i+j}, \quad j = -1, 1. \\ &\int_{I_{i+j}} \frac{q_1(x)}{\Delta x} dx = \bar{u}_{i+j}, \quad j = -1, 0, \qquad \int_{I_{i+j}} \frac{q_2(x)}{\Delta x} dx = \bar{u}_{i+j}, \quad j = 0, 1. \end{aligned} \tag{2.10}$$

Then, the smoothness of the functions $q_0(x), q_1(x), q_2(x)$ in the cell I_i is measured with the smoothness indicators $\beta_0, \beta_1, \beta_2$:

$$\beta_m = \sum_{\kappa=1}^{r} \Delta x^{2\kappa - 1} \int_{I_i} \Big(\frac{d^\kappa}{dx^\kappa} q_m(x) \Big)^2 dx, \quad m = 0, 1, 2. \tag{2.11}$$

where r is the degree of polynomials $q_m(x)$.

We measure the absolute difference between β_0, β_1 and β_2 by introducing a new parameter τ, then define nonlinear weights as following:

$$\begin{aligned} &\omega_m = \frac{\tilde{\omega}_m}{\sum_{m=0}^{2} \tilde{\omega}_m}, \quad \tilde{\omega}_m = r_m \Big(1 + \frac{\tau}{\varepsilon + \beta_m} \Big), \\ &\tau = \left(\frac{|\beta_1 - \beta_2| + |\beta_1 - \beta_3|}{2} \right)^2, \quad m = 0, 1, 2. \end{aligned} \tag{2.12}$$

where we take $\epsilon = 10^{-6}$ to avoid zero in the denominator in this paper.

For two dimensional case, we use the same troubled-cell indicator as above. This procedure is employed dimensional by dimensional manner. In x-direction, $\bar{u}_{i+1,j}, \bar{u}_{i,j}, \bar{u}_{i-1,j}, \bar{v}_{i,j}$ are used while $\bar{u}_{i,j+1}, \bar{u}_{i,j}, \bar{u}_{i,j-1}, \bar{w}_{i,j}$ are used in y-direction. The cell $I_{i,j}$ is identified as a trouble-cell whether it is marked in x or y direction.

If the cell $\square_0$ is marked as troubled-cell, then we modify the first order moment in this cell. We apply with the same modification procedure in one-dimensional case, also dimensional by dimensional manner. That is, we modify $\bar{v}_{i,j}$ with $\bar{u}_{i+1,j}, \bar{u}_{i,j}, \bar{u}_{i-1,j}, \bar{v}_{i+1,j}, \bar{v}_{i-1,j}$, and employ $\bar{u}_{i,j+1}, \bar{u}_{i,j}, \bar{u}_{i,j-1}, \bar{w}_{i,j+1}, \bar{w}_{i,j-1}$ to modify $\bar{w}_{i,j}$.

Step 2. The hybrid HWENO reconstruction procedure for $u^{\pm}(P_{lk}, t)$ and $\nabla u^{\pm}(P_{lk}, t)$.

If the cell $\square_0$ is marked as a troubled-cell, then we use above modified first-order moment information in the HWENO reconstruction for u and it's gradients ∇u. The fifth-order finite volume HWENO mythology [49] is applied for this reconstruction process.

In one-dimensional case, the big stencil is taken as $S_0 = \{I_{i-1}, I_i, I_{i+1}\}$ while the two small stencils are set to $S_1 = \{I_{i-1}, I_i\}$, $S_2 = \{I_i, I_{i+1}\}$. On these stencils, we obtain polynomials $q_0(x), q_1(x), q_2(x)$, satisfying:

$$\begin{aligned}
&\int_{I_{i+j}} \frac{q_0(x)}{\Delta x} dx = \bar{u}_{i+j}, \quad \int_{I_{i+j}} q_0(x) \frac{x - x_{i+j}}{\Delta x^2} dx = \bar{v}_{i+j}, \quad j = -1, 0, 1, \\
&\int_{I_{i+j}} \frac{q_1(x)}{\Delta x} dx = \bar{u}_{i+j}, \quad \int_{I_i} q_1(x) \frac{x - x_i}{\Delta x^2} dx = \bar{v}_i, \qquad j = -1, 0, \\
&\int_{I_{i+j}} \frac{q_2}{\Delta x} dx = \bar{u}_{i+j}, \quad \int_{I_i} q_2(x) \frac{x - x_i}{\Delta x^2} dx = \bar{v}_i, \qquad j = 0, 1.
\end{aligned} \tag{2.13}$$

where the linear weights r_0, r_1, r_2 are any set of positive numbers with condition $\sum_{m=0}^{2} r_m = 1$. So we have the final HWENO reconstruction polynomial:

$$Q(x) = \omega_0 \Big(\frac{1}{r_0} q_0(x) - \frac{r_1}{r_0} q_1(x) - \frac{r_2}{r_0} q_2(x) \Big) + \omega_1 q_1(x) + \omega_2 q_2(x), \tag{2.14}$$

where nonlinear weights $\omega_0, \omega_1, \omega_2$ and the parameter τ are also defined as in (2.12). We calculate the smoothness indicators $\beta_0, \beta_1, \beta_2$ with (2.11) to measure the smoothness of the functions $q_0(x), q_1(x), q_2(x)$ in the cell I_i, intending to maintain the same high order computational accuracy in the smooth region and non-oscillatory property near discontinuity.

After this, we finally obtain the HWENO approximation for function and derivatives at the cell interface of I_i by:

$$u^-_{i+\frac{1}{2}} = Q(x_{i+\frac{1}{2}}), \quad u^+_{i-\frac{1}{2}} = Q(x_{i+\frac{1}{2}}), \quad (u^-_x)_{i+\frac{1}{2}} = Q'(x_{i+\frac{1}{2}}), \quad (u^+_x)_{i-\frac{1}{2}} = Q'(x_{i-\frac{1}{2}}). \tag{2.15}$$

The volume integral terms of equation (2.2) are approximated by 3-point Gaussian integration, such as: $\omega_1 = \frac{5}{18}$, $\omega_2 = \frac{4}{9}$, $\omega_3 = \frac{5}{18}$ are the quadrature weights, and the Gaussian point coordinates are $P_1 = x_{i-\frac{\sqrt{15}}{10}}$, $P_2 = x_i$, $P_3 = x_{i+\frac{\sqrt{15}}{10}}$. The function and derivative values at these Gauss-point values can be obtained directly by $q_0(P_k)$, $\frac{dq_0}{dx}(P_k)$, $k = 1, 2, 3$.

If the cell I_i is not marked as troubled-cell, then the reconstruction processes is implemented by only using the linear approximation. So it is reasonable to use the highest degree polynomial $q_0(x)$, so that $u^-_{i+\frac{1}{2}} = q_0(x_{i+\frac{1}{2}})$, $(u^-_x)_{i+\frac{1}{2}} = q_0'(x_{i+\frac{1}{2}})$, respectively.

In two-dimensional case, we need to reconstruct the point values $u^{\pm}(P_{lk}, t)$ and $u^{\pm}_x(P_{lk}, t), u^{\pm}_y(P_{lk}, t)$ on the cell $I_{i,j}$ based on the formula (2.5) and (2.6).

For the HWENO scheme, we take big stencil S_0 as in Fig. 1 and construct quartic polynomial $q_0(x, y)$. For four small stencils, we take $S_m, m = 1, 2, 3, 4$ as in Fig. 2, and construct respective quadratic polynomial $q_m(x, y), m = 1, 2, 3, 4$.

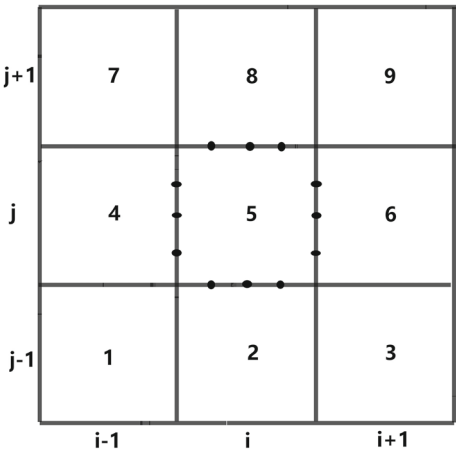

Fig. 1 The big stencil S_0 and it's new labels

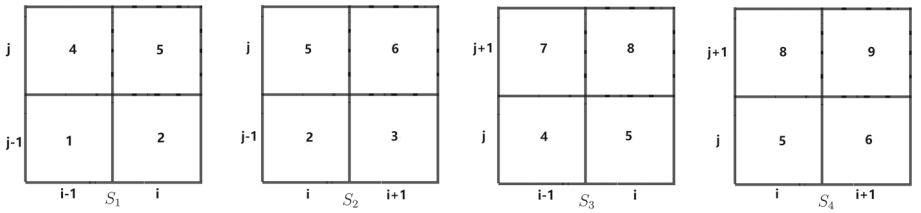

Fig. 2 The four small stencils and their corresponding labels

With the assist of these polynomials, we can obtain the final HWENO reconstruction polynomial $Q(x, y)$ as:

$$Q(x, y) = \omega_0\Big(\frac{1}{r_0}q_0(x, y) - \sum_{m=1}^{4}\frac{r_m}{r_0}q_m(x, y)\Big) + \sum_{m=1}^{4}\omega_m q_m(x, y). \tag{2.16}$$

with any set of artificial positive linear weights with condition $\sum_{m=0}^{4} r_m = 1$. These polynomials satisfy the conditions in following:

$$\begin{aligned} &\int_{I_n}\frac{q_m(x, y)}{\Delta x\Delta y}dxdy = \bar{u}_n, \\ &\int_{I_{n_x}} q_m(x, y)\frac{x - x_{n_x}}{\Delta x^2\Delta y}dxdy = \bar{v}_{n_x}, \quad \int_{I_{n_y}} q_m(x, y)\frac{y - y_{n_y}}{\Delta x\Delta y^2}dxdy = \bar{w}_{n_y}. \end{aligned} \tag{2.17}$$

for

$$\begin{aligned} &m = 0, \quad n = 1, 2, 3, 4, 5, 6, 7, 8, 9, \quad n_x = n_y = 2, 4, 5, 6, 8; \\ &m = 1, \quad n = 1, 2, 4, 5, \quad n_x = n_y = 5; \qquad m = 2, \quad n = 2, 3, 5, 6, \quad n_x = n_y = 5; \\ &m = 3, \quad n = 4, 5, 7, 8, \quad n_x = n_y = 5; \qquad m = 4, \quad n = 5, 6, 8, 9, \quad n_x = n_y = 5; \end{aligned}$$

We can obtain the quartic polynomial $q_0(x, y)$ with the matching requirement of the zero-order moments on the stencil S_0, the first-order moments on the cell $I_{i,j}$ while the others can be obtained in the least square sense [21]. The expressions of four quadratic polynomials $q_m(x, y), m = 1, 2, 3, 4$ can directly obtain by requirements in (2.17), respectively.

We compute the smoothness indicators $\beta_m (m = 0, 1, 2, 3, 4)$ to measure the smoothness of the function $q_m(x, y)$ in the target cell $I_{i,j}$ as:

$$\beta_m = \sum_{|\kappa|=1}^{r} |I_{i,j}|^{|\kappa|-1} \int_{I_{i,j}} \left(\frac{\partial^{|\kappa|}}{\partial x^{\kappa_1} \partial y^{\kappa_2}} q_m(x, y) \right)^2 dxdy, \qquad m = 0, 1, 2, 3, 4. \tag{2.18}$$

where r is the degree of $q_m(x, y)$ and $\kappa = (\kappa_1, \kappa_2)$, $|\kappa| = \kappa_1 + \kappa_2$. We introduce a new parameter τ to define the absolute difference between $\beta_m (m = 0, 1, 2, 3, 4)$ and define nonlinear weights as following:

$$\tau = \left(\frac{\sum_{m=1}^{4} |\beta_0 - \beta_m|}{4} \right)^2, \quad \tilde{\omega}_m = r_m \left(1 + \frac{\tau}{\varepsilon + \beta_m} \right), \quad \omega_m = \frac{\tilde{\omega}_m}{\sum_{l=0}^{4} \tilde{\omega}_m}, \tag{2.19}$$

in which $\epsilon = 10^{-6}$. The HWENO reconstruction of the solution u at the interface points is:

$$u^*(P_{lk}, t) = Q(P_{lk}) = \omega_0 \left(\frac{1}{r_0} q_0(P_{lk}) - \sum_{m=1}^{4} \frac{r_m}{r_0} q_m(P_{lk}) \right) + \sum_{m=1}^{4} \omega_m q_m(P_{lk}), \tag{2.20}$$

where " $*$ " represents " $+$ " when P_{lk} is placed on the bottom or left interface of $I_{i,j}$, and " $*$ " represents " $-$ " on the top or right interface of $I_{i,j}$. The final HWENO reconstruction of the derivative values at point (P_{lk}, t) are:

$$\begin{aligned} u_x^*(P_{lk}, t) &= \frac{\partial Q(P_{lk})}{\partial x} = \omega_0 \left(\frac{1}{r_0} \frac{\partial q_0(P_{lk})}{\partial x} - \sum_{m=1}^{4} \frac{r_m}{r_0} \frac{\partial q_m(P_{lk})}{\partial x} \right) + \sum_{m=1}^{4} \omega_m \frac{\partial q_m(P_{lk})}{\partial x}, \\ u_y^*(P_{lk}, t) &= \frac{\partial Q(P_{lk})}{\partial y} = \omega_0 \left(\frac{1}{r_0} \frac{\partial q_0(P_{lk})}{\partial y} - \sum_{m=1}^{4} \frac{r_m}{r_0} \frac{\partial q_m(P_{lk})}{\partial y} \right) + \sum_{m=1}^{4} \omega_m \frac{\partial q_m(P_{lk})}{\partial y}. \end{aligned} \tag{2.21}$$

The 3×3 Gauss points are located as in Fig. 1, such as the quadrature weights are $\omega_1 = \frac{5}{18}$, $\omega_2 = \frac{4}{9}$, $\omega_3 = \frac{5}{18}$, and the Gaussian point coordinates in x and y direction are $P_{x_1} = x_{i-\frac{\sqrt{15}}{10}}$, $P_{x_2} = x_i$, $P_{x_3} = x_{i+\frac{\sqrt{15}}{10}}$ and $P_{y_1} = y_{j-\frac{\sqrt{15}}{10}}$, $P_{y_2} = y_j$, $P_{y_3} = y_{j+\frac{\sqrt{15}}{10}}$. As is the same in one-dimensional case, the volume integrals in (2.2) are approximated by Gaussian integration, and the Gauss point values are obtained directly by $q_0(P_{x_{k_1}}, P_{y_{k_2}}), k_1, k_2 = 1, 2, 3$.

The above HWENO procedure is used on the cell $I_{i,j}$ if it is marked as troubled-cell. Otherwise, the values of solution u and derivative at point P_{lk} are approximated directly by $q_0(P_{lk})$, $\frac{\partial q_0(P_{lk})}{\partial x}$ and $\frac{\partial q_0(P_{lk})}{\partial y}$, respectively.

3 Time Discretization

So far, only spatial discretization has been considered. The Eq. (2.1) is equal to the first order ordinary differential equation(ODE) after spatial discretization discussed above as:

$$\frac{du}{dt} = L(u). \tag{3.1}$$

Any suitable ODE solvers can be applied on this ODE system. Here we apply the third order total variation diminishing Runge–Kutta (TVD-RK3) method [18] to solve (3.1), which

is given as

$$\begin{aligned} u^{(1)} =& u^n + \Delta t L(u^n), \\ u^{(2)} =& \frac{3}{4}u^n + \frac{1}{4}\big(u^{(1)} + \Delta t L(u^{(1)})\big), \\ u^{n+1} =& \frac{1}{3}u^n + \frac{2}{3}\big(u^{(2)} + \Delta t L(u^{(2)})\big). \end{aligned} \tag{3.2}$$

The TVD-RK3 method has the ability of maintaining nonlinear stability. For advection-diffusion equations, it is not the only solver works well, but could still be a appropriate choice. The time step Δt must satisfies the Courant-Friedrich-Lewy (CFL) stability condition in order to ensure numerical stability of the scheme.

To determine the CFL condition, we consider the linear advection-diffusion equation

$$u_t + au_x = bu_{xx}. \tag{3.3}$$

with the fifth order linear approximation in spatial direction and the TVD-RK3 method in time direction. For the HWENO scheme with TVD-RK3 method to solve (3.3), it is required that the time step restriction $\Delta t \leq \frac{1}{\frac{\max|F'(u)|}{\mathrm{CFL}_a \Delta x} + \frac{\max|G'(u)|}{\mathrm{CFL}_b \Delta x^2}}$, where $F(u) = au, G(u) = bu$ and CFL_a is the CFL condition for $u_t + au_x = 0$ while CFL_b is the CFL condition for $u_t = bu_{xx}$.

Evaluating the numerical fluxes $\hat{F}_{i+\frac{1}{2}}, \hat{G}_{i+\frac{1}{2}}$ at $x_{i+\frac{1}{2}}$, and obtaining $\hat{F}_{i-\frac{1}{2}}, \hat{G}_{i-\frac{1}{2}}$ by shifting the index with -1, insert these in (2.2) after Fourier transform, we have:

$$\frac{d}{dt}\begin{pmatrix} \tilde{u} \\ \tilde{v} \end{pmatrix} = \mathcal{A}\begin{pmatrix} \tilde{u} \\ \tilde{v} \end{pmatrix}, \tag{3.4}$$

By applying the TVD-RK3 method for (3.4), we can obtain the amplification matrix and it's two eigenvalues. From the stability analysis and direct calculation, we obtain $\mathrm{CFL}_a = 0.844$ in the case of $a = 1, b = 0$ for (3.3) while $\mathrm{CFL}_b = 0.1282$ in the case of $a = 0, b = 1$. Considering the stability of nonlinear advection-diffusion equation, we take $\mathrm{CFL} = \min(\mathrm{CFL}_a, \mathrm{CFL}_b) = \mathrm{CFL}_b$ in general. So we get the CFL restriction as:

$$0 < \mathrm{CFL} = \Delta t\left(\frac{\max|F'(u)|}{\Delta x} + \frac{\max|G'(u)|}{\Delta x^2}\right) \leq 0.1282. \tag{3.5}$$

4 Numerical Tests

We conclude this paper with numerical verification for some one- and two-dimensional diffusion and advection-diffusion equations.

For one-dimensional advection-diffusion equations

$$u_t + F(u)_x = G(u)_{xx}, \tag{4.1}$$

the time step is set as $\Delta t = \frac{CFL}{\frac{\max|F'(u)|}{\Delta x} + \frac{\max|G'(u)|}{\Delta x^2}}$. While for two-dimensional problems

$$u_t + F_1(u)_x + F_2(u)_y = G_1(u)_{xx} + G_2(u)_{yy}, \tag{4.2}$$

the time step is taken as $\Delta t = \frac{CFL}{\frac{\max|F_1'(u)|}{\Delta x} + \frac{\max|F_2'(u)|}{\Delta y} + \frac{\max|G_1'(u)|}{\Delta x^2} + \frac{\max|G_2'(u)|}{\Delta y^2}}$.

We take CFL=0.12 for all numerical simulation for hybrid HWENO scheme in this paper. For all following one and two dimensional tests which contain the convection term, we

apply the same fifth-order HWENO reconstruction [49] to discretize the advection term with Lax-Friedrichs flux. For the propose of fair comparison with DWENO [32] and MRWENO [24] schemes, we modify DWENO and MRWENO schemes to hybrid DWENO and hybrid MRWENO schemes with new the troubled-cell indicator (4.3) based on nodal point information. The CFL number is set to be 0.4 for hybrid DWENO and hybrid MRWENO schemes. The troubled-cell indicator for DWENO and MRWENO is defined as:

$$\mathcal{I}(u_{i-1}, u_i, u_{i+1}) = \begin{cases} 1, & \tau > c_1 \Delta x^{c_2} \max\{\beta_1, \beta_2\}, \\ 0, & \text{Otherwise.} \end{cases} \tag{4.3}$$

where β_1, β_2 and τ are defined as:

$$\beta_1 = (u_i - u_{i-1})^2, \quad \beta_2 = (u_{i+1} - u_i)^2, \quad \tau = \big(\beta_1 - \beta_2\big)^2. \tag{4.4}$$

and the two parameters c_1 and c_2 are determined as in Sect. 2. When $\mathcal{I} = 1$, the cell I_i would be marked as troubled-cell.

To clarify, the combination of fifth order finite difference WENO scheme [23] with the Lax-Friedrichs flux splitting and DWENO [32] scheme is considered in [32] to solve advection-diffusion problems, while the combination of fifth order multi-resolution WENO method [53] and MRWENO [24] scheme is used to solve advection-diffusion equation in [24]. This is still the case during comparison in this paper for these two schemes.

When the diffusion term is written as $(a(u)u_x)_x$, an equivalent form can be rewritten as $g(u)_{xx}$. We employ DDG coefficient $b_0 = 1$ for all one and two-dimensional tests. The numerical solutions in the figures of the present scheme below are based on the cell-averages.

Example 1 We consider the convection-diffusion equation:

$$u_t + u_x = u_{xx}, \quad 0 \le x \le 2\pi. \tag{4.5}$$

with the initial condition $u(x, 0) = \sin(x)$ and periodic boundary condition. The exact solution is $u(x, t) = e^{-t} \sin(x - t)$.

The L_1, L_2, L_∞ errors and convergency results at $T = 1$ in domain $x \in [0, 2\pi]$ are shown in Table 1 and compared with hybrid DWENO and hybrid MRWENO scheme. We can see that the numerical errors by hybrid HWENO scheme are smaller than those by hybrid DWENO and hybrid MRWENO schemes with the same meshes.

Moreover, we compare the CPU cost against numerical errors in Fig. 3 for hybrid DWENO, hybrid MRWENO and hybrid HWENO scheme. It can be observed that the hybrid HWENO scheme is more efficient than hybrid DWENO and hybrid MRWENO scheme.

Example 2 We compute the diffusion equation to measure the computational accuracy of present scheme for one-dimensional smooth diffusion problem:

$$u_t = u_{xx}, \quad -\pi \le x \le \pi. \tag{4.6}$$

with the initial condition $u(x, 0) = \sin(x)$ and periodic boundary condition. The exact solution is $u(x, t) = e^{-t} \sin(x)$.

Table 2 gives the errors and sixth order of convergency results in terms of L_1, L_2 and L_∞ norms at $T = 2$ in $x \in [-\pi, \pi]$ and compare the results with hybrid DWENO and hybrid MRWENO schemes. The proposed scheme has comparable accuracy with that of hybrid DWENO and MRWENO schemes. If the discontinues problem is considered, then the modification of first order moment is required, and we can obtain fifth-order accuracy in general.

Table 1 The comparison of errors and rates of convergence of different numerical schemes at $T = 1$ for Example 1

	Hybrid HWENO		Hybrid DWENO		Hybrid MRWENO	
N	L_∞	Order	L_∞	Order	L_∞	order
20	2.1861e–08		1.6111e–05		1.6111e–05	
40	1.0804e–10	7.6606	5.3596e–07	4.9097	5.3596e–07	4.9097
80	3.0833e–12	5.1310	1.7415e–08	4.9437	1.7415e–08	4.9437
160	3.6693e–14	6.3928	5.5728e–10	4.9658	5.5728e–10	4.9658
N	L_1	Order	L_1	Order	L_1	Order
20	1.4135e–08		1.0548e–05		1.0548e–05	
40	6.8994e–11	7.6786	3.4436e–07	4.9369	3.4436e–07	4.9369
80	1.9637e–12	5.1348	1.1135e–08	4.9507	1.1135e–08	4.9507
160	2.2563e–14	6.4435	3.5550e–10	4.9692	3.5550e–10	4.9692
N	L_2	Order	L_2	Order	L_2	Order
20	1.5636e–08		1.1632e–05		1.1632e–05	
40	7.6561e–11	7.6741	3.8162e–07	4.9299	3.8162e–07	4.9299
80	2.1806e–12	5.1338	1.2352e–08	4.9493	1.2352e–08	4.9493
160	2.5084e–14	6.4418	3.9461e–10	4.9682	3.9461e–10	4.9682

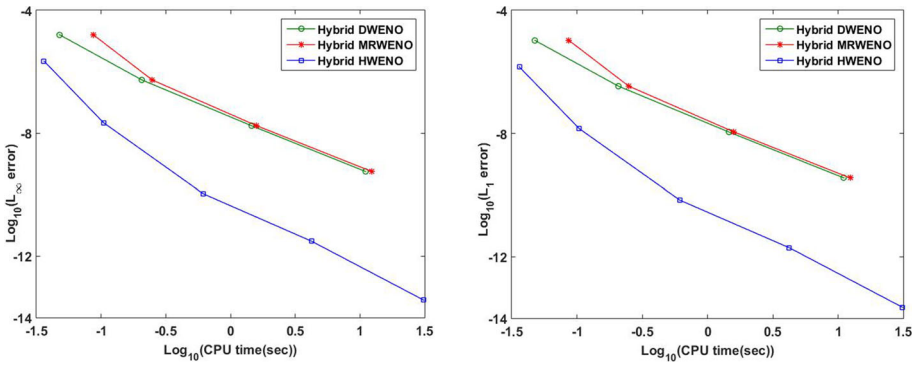

Fig. 3 CPU time against L_∞ error(left) and CPU time against L_1 error(right) between hybrid DWENO, hybrid MRWENO and hybrid HWENO scheme for Example 1

We show numerical errors against CPU cost by these three schemes in Fig. 4, which shows the hybrid DWENO and hybrid MRWENO schemes have slightly better efficiency than hybrid HWENO scheme. This is actually reasonable since hybrid HWENO scheme solves two equations instead of one, as a result achieve better accuracy in the simulation.

In above two numerical tests, there is no troubled-cell is marked, therefore, all computation is based on linear approximation for all three schemes. Overall, the efficiency results for advection-diffusion and diffusion equations indicates that the hybrid HWENO scheme achieves smaller numerical errors and requires a little much computational time than hybrid DWENO and MRWENO schemes.

Table 2 The comparison of errors and rates of convergence of different numerical schemes at $T = 2$ for Example 2

	Hybrid HWENO		Hybrid DWENO		Hybrid MRWENO	
N	L_∞	Order	L_∞	Order	L_∞	Order
10	3.9461e–06		1.9512e–05		1.9512e–05	
20	6.8756e–08	5.8428	2.5192e–07	6.2753	2.5192e–07	6.2753
40	1.0930e–09	5.9751	3.6702e–09	6.1010	3.6702e–09	6.1010
80	1.7178e–11	5.9916	5.6321e–11	6.0260	5.6321e–11	6.0260
N	L_1	Order	L_1	Order	L_1	Order
10	2.5540e–06		1.1480e–05		1.1480e–05	
20	4.3450e–08	5.8772	1.5148e–07	6.2439	1.5148e–07	6.2439
40	6.9453e–10	5.9672	2.2748e–09	6.0572	2.2748e–09	6.0572
80	1.0930e–11	5.9896	3.5394e–11	6.0061	3.5394e–11	6.0061
N	L_2	Order	L_2	Order	L_2	Order
10	2.9120e–06		1.3832e–05		1.3832e–05	
20	4.8619e–08	5.9043	1.7384e–07	6.3141	1.7384e–07	6.3141
40	7.7290e–10	5.9751	2.5634e–09	6.0836	2.5634e–09	6.0836
80	1.2146e–11	5.9917	3.9579e–11	6.0172	3.9579e–11	6.0172

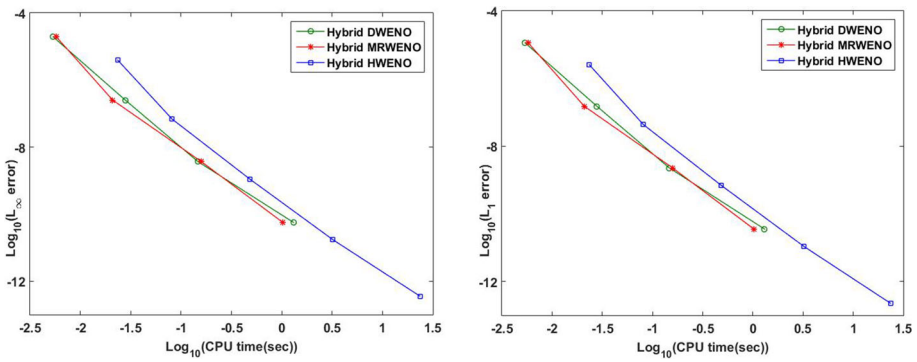

Fig. 4 CPU time versus L_∞ error(left) and CPU time versus L_1 error(right) between hybrid DWENO, hybrid MRWENO and hybrid HWENO scheme for Example 2

Example 3 We compute the Barenblatt solution of porous medium found by Zel'dovich and Kompaneetz (see [7, 33, 46]) as:

$$\begin{cases} u_t = (u^m)_{xx}, & x \in [-6,6], \\ B_m(x,t) = \frac{1}{t^k}\left[\left(1 - \frac{k(m-1)}{2m}\frac{|x|^2}{t^{2k}}\right)_+\right]^{\frac{1}{m-1}}, \ u_+ = \max(u,0), \quad m > 1, \quad k = \frac{1}{m+1}. \end{cases} \tag{4.7}$$

We choose $t = 1$ as the initial time and the computation domain $[-6, 6]$ with zero boundary condition $u(\pm 6, t) = 0$.

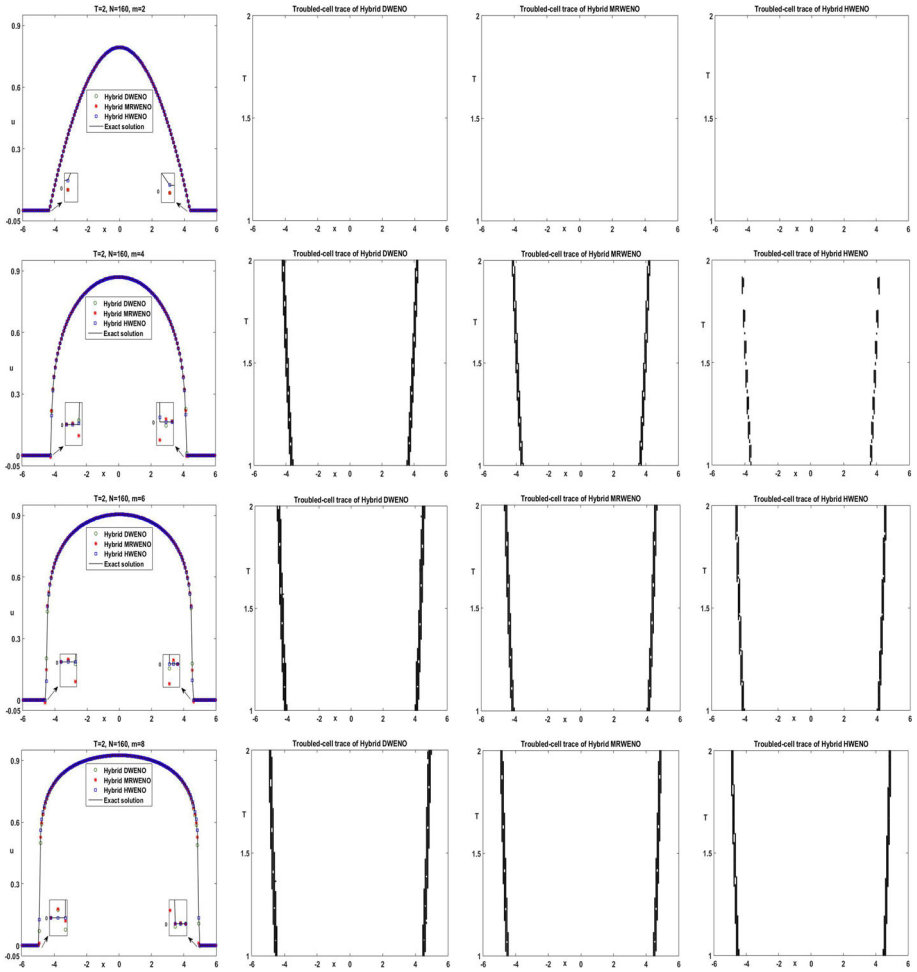

Fig. 5 Numerical solution of PME equation for $m = 2, 4, 6, 8$ and solution comparison with hybrid DWENO and MRWENO scheme at $T = 2$ for Example 3(left), corresponding troubled-cell(right three)

The Barenblatt solution for different value of m can be simulated sharply and accurately without noticeable oscillations near the interface with present scheme. The numerical solution is compared with the results of hybrid DWENO, hybrid MRWENO schemes in Fig. 5(left), and all three types of schemes give very similar results without oscillation. Yet the superiority of the present scheme can be observed in the enlarged image. In Fig. 5(right three), we also plotted the trajectory of the troubled-cell of these three schemes.

In order to observe the two-box colliding case with the same heights, we choose the initial condition as:

$$u(x,0) = \begin{cases} 1, & x \in (0.7, 3.7) \cup (-3.7, -0.7), \\ 0, & \text{otherwise.} \end{cases} \tag{4.8}$$

This example simulates the temperature change of medium when two hot spots are placed in the computational domain. The numerical solution of the PME equation with $m = 5$ is

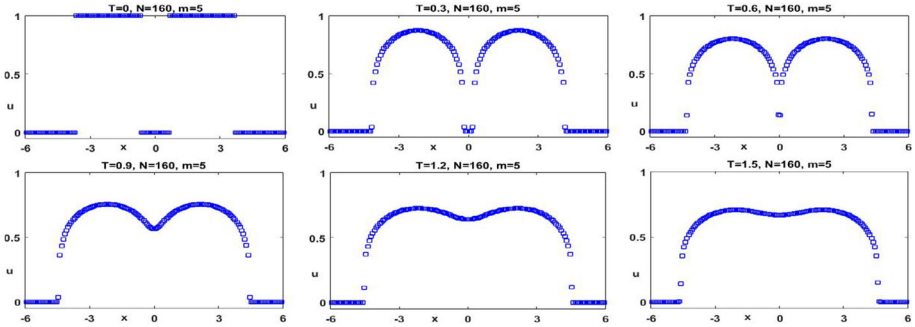

Fig. 6 Same hight two-box collision case of PME equation when $m = 5$ for Example 3

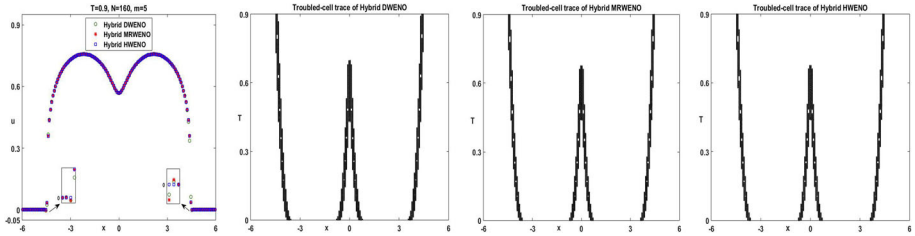

Fig. 7 Comparison of hybrid DWENO, hybrid MRWENO and hybrid HWENO schemes for two-box with same hight collision case of PME equation when $m = 5$ for Example 3(left) at $T = 0.9$ and troubled-cell tract(right three)

plotted in Fig. 6 on varies time level. From Fig. 7(left), we can observe that the temperature balance is more clear with present scheme than hybrid DWENO and hybrid MRWENO scheme, which highlights the compact property of the hybrid HWENO scheme. The trajectory of troubled-cell of these three different hybrid schemes are also given in Fig. 7(right three).

In order to observe the collision of two boxes with the different heights, we take the initial condition as:

$$u(x,0) = \begin{cases} 2, & x \in (0,3), \\ 1, & x \in (-4,-1), \\ 0, & \text{otherwise}. \end{cases} \tag{4.9}$$

We plot the numerical evolution of the PME equation with $m = 6$ in Fig. 8 on various time levels. The compact property of hybrid HWENO scheme also can be seen in Fig. 9 while almost the same amount of troubled-cells are marked for each scheme. From Figs. 6 and 8, it can be observed that the two-boxes move outward independently at first, and collide. Regardless of the heights of the two boxes are the same in the initial condition, they eventually connect to each other, allowing the temperature to level off.

Example 4 Considering the scalar advection-diffusion Buckley–Leverett equation:

$$u_t + F(u)_x = \varepsilon\big(v(u)u_x\big)_x, \quad x \in [0,1], \quad \varepsilon v(u) \geq 0. \tag{4.10}$$

In current test case, we take $\varepsilon = 0.01$. The advection flux $F(u)$ has an S-shaped form

$$F(u) = \frac{u^2}{2u^2 - 2u + 1}, \tag{4.11}$$

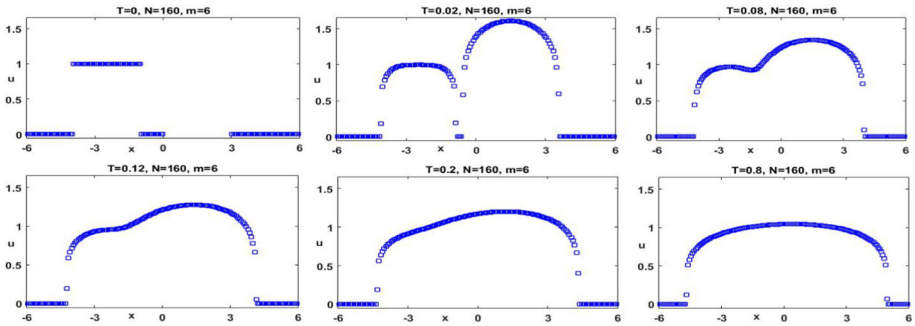

Fig. 8 Same hight two-box collision case of PME equation when $m = 5$ for Example 3

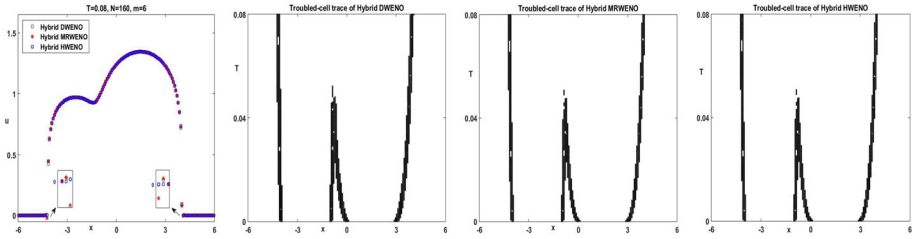

Fig. 9 Comparison of hybrid DWENO, hybrid MRWENO and hybrid HWENO schemes for two-box with different hight collision case of PME equation when $m = 6$ for Example 3(left) at $T = 0.08$ and troubled-cell tract (right three)

and

$$v(u) = \begin{cases} 4u(1-u), & 0 \le u \le 1, \\ 0, & \text{otherwise.} \end{cases} \tag{4.12}$$

so we can derive the explicit formulation of $G(u)$ by direct integration as:

$$G(u) = \begin{cases} 0, & u < 0, \\ \varepsilon(2u^2 - \frac{4}{3}u^3), & 0 \le u \le 1, \\ \frac{2\varepsilon}{3}, & u > 1. \end{cases} \tag{4.13}$$

We consider the initial data as:

$$u(x,0) = \begin{cases} 0, & \frac{1}{3} < x \le 1, \\ 1 - 3x, & 0 \le x \le \frac{1}{3}. \end{cases} \tag{4.14}$$

and the inflow and outflow boundary conditions for this example.

The numerical solution for different numbers of grid points at $T = 0.2$ are computed in Fig. 10(up left). Similar numerical waves with $N = 200$ spatial grid points are plotted in Fig. 10(up right) with hybrid DWENO and hybrid MRWENO scheme. Our scheme develops better results in sensitive points, which converge more accurately to the correct entropy solution. On the bottom of Fig. 10, we also plot the track of troubled-cell of three different hybrid schemes.

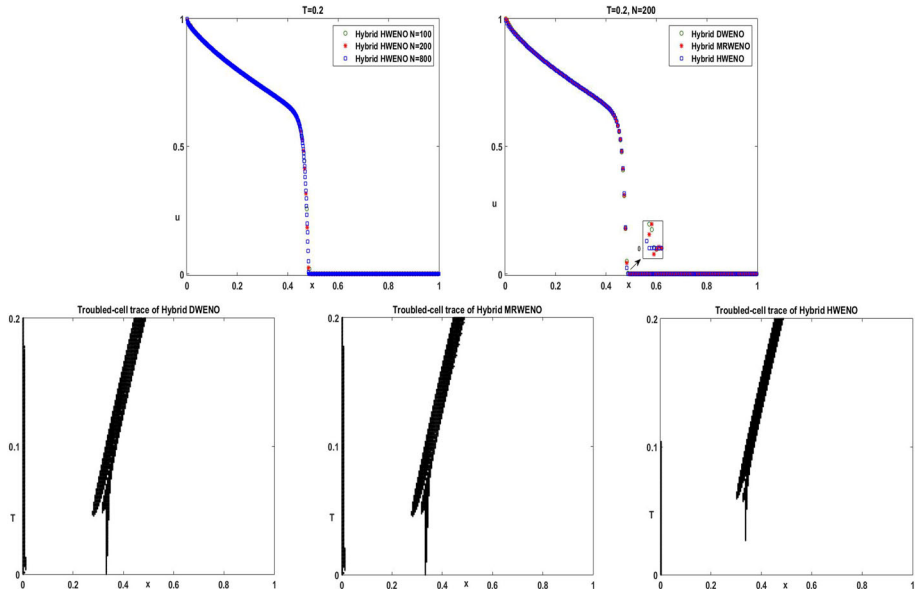

Fig. 10 Numerical solution of Buckley–Leverett equation (4.10) at $T = 0.2$ in $x \in [0, 1]$ with (4.11),(4.13) and initial condition (4.14) for Example 4(up left), solution comparison with hybrid DWENO and MRWENO scheme(up right) and corresponding troubled-cell of hybrid DWENO(bottom left), hybrid MRWENO(bottom middle), hybrid HWENO(bottom right)

To observe the gravitational effects on Buckley–Leverett equation, we consider convection flux (4.11), diffusion flux (4.13), and with the initial data representing a Riemann problem:

$$u(x,0) = \begin{cases} 1, & 1 - \frac{1}{\sqrt{2}} \le x \le 1, \\ 0, & 0 \le x < 1 - \frac{1}{\sqrt{2}}. \end{cases} \tag{4.15}$$

Figure 11(up left) shows that the present scheme produces numerical solutions for different numbers of grid points at $T = 0.2$ without noticeable oscillation for the Riemann problem with gravitational effect accurately. It can be observed from Fig. 11(up right) that hybrid HWENO scheme is more closer to zero around point $x = 0.245$ while other two schemes develop negative results around this point. The linear approximation accounts for the main part of the calculation according to the Fig. 11(bottom three) for all three hybrid schemes.

To observe the non-gravitational effects on Buckley–Leverett equation, we consider diffusion flux (4.13), the initial data (4.15), and the convection flux:

$$F(u) = \frac{u^2}{2u^2 - 2u + 1}\big(-5u^2 + 10u - 4\big). \tag{4.16}$$

In Fig. 12(up left), we plot numerical solution without gravitational effect. It can be observed that present scheme also provide good result in this case under various grid meshes. In Fig. 12(up right), we also can find the compatible advantages of the HWENO scheme. The troubled-cells of three hybrid schemes in the entire computational process are also can be seen in Fig. 12(bottom three).

Example 5 Considering the strongly degenerate parabolic advection-diffusion equation

$$u_t + F(u)_x = \varepsilon\big(v(u)u_x\big)_x, \quad x \in [-2, 2], \quad \varepsilon v(u) \ge 0. \tag{4.17}$$

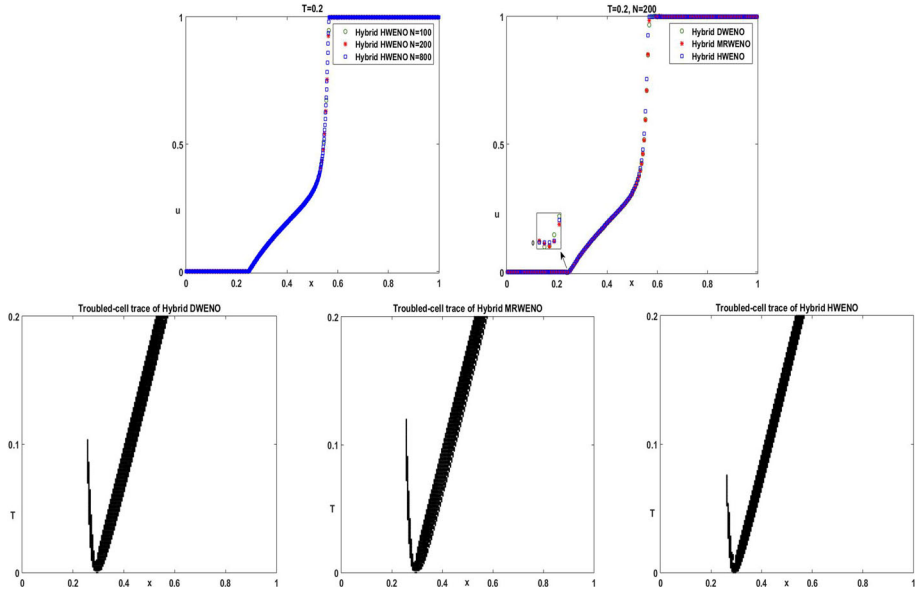

Fig. 11 Riemann problem of Buckley–Leverett equation (4.10) with gravitational effect at $T = 0.2$ in $x \in [0, 1]$ with (4.11),(4.13) and initial condition (4.15) for Example 4(up left), solution comparison with hybrid DWENO and MRWENO scheme(up right) and corresponding troubled-cell of hybrid DWENO(bottom left), hybrid MRWENO(bottom middle), hybrid HWENO(bottom right)

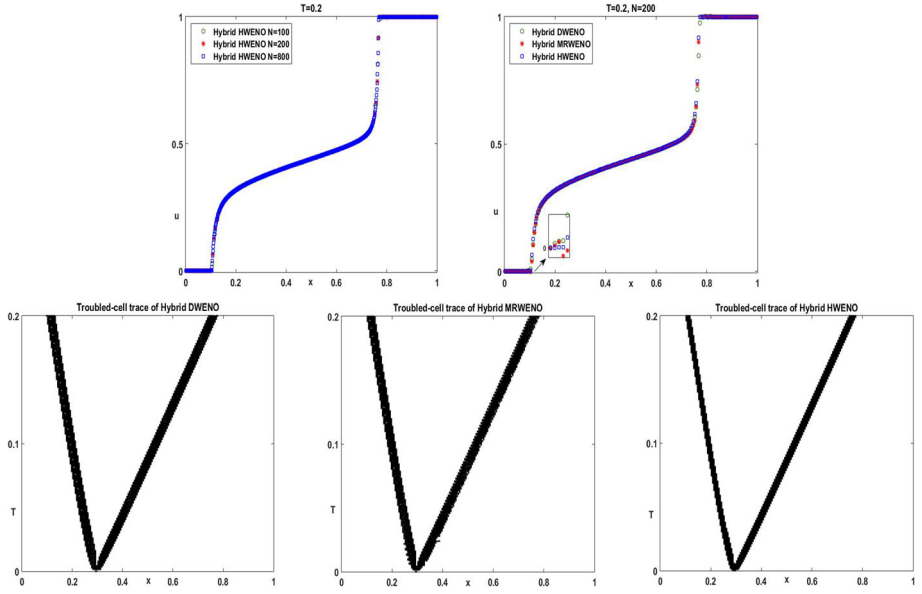

Fig. 12 Riemann problem of Buckley–Leverett equation (4.10) without gravitational effect at $T = 0.2$ in $x \in [0, 1]$ with (4.16),(4.13) and initial condition (4.15) for Example 4(up left), solution comparison with hybrid DWENO and MRWENO scheme(up right) and corresponding troubled-cell of hybrid DWENO(bottom left), hybrid MRWENO(bottom middle), hybrid HWENO(bottom right)

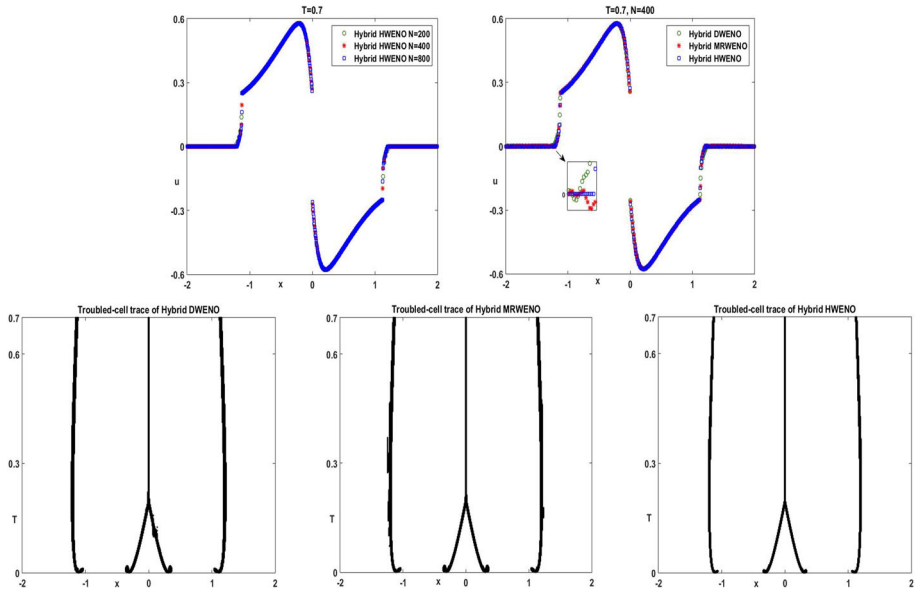

Fig. 13 Numerical solution of strongly degenerate parabolic convection-diffusion equation at $T = 0.7$ for Example 5(up left), solution comparison with hybrid DWENO and MRWENO scheme(up right) and corresponding troubled-cell of hybrid DWENO(bottom left), hybrid MRWENO(bottom middle), hybrid HWENO(bottom right)

We take $F(u) = u^2$, $\varepsilon = 0.1$, and

$$v(u) = \begin{cases} 1, & |u| > \frac{1}{4}, \\ 0, & |u| \leq \frac{1}{4}. \end{cases} \tag{4.18}$$

The explicit formulation of $G(u)$ can be written as:

$$G(u) = \begin{cases} \varepsilon\left(u - \frac{1}{4}\right), & u > \frac{1}{4}, \\ \varepsilon\left(u + \frac{1}{4}\right), & u < -\frac{1}{4}, \\ 0, & |u| \leq \frac{1}{4}. \end{cases} \tag{4.19}$$

The initial data is taken as

$$u(x,0) = \begin{cases} -1, & \frac{1}{\sqrt{2}} - \frac{2}{5} < x < \frac{1}{\sqrt{2}} + \frac{2}{5}, \\ 1, & -\frac{1}{\sqrt{2}} - \frac{2}{5} < x < -\frac{1}{\sqrt{2}} + \frac{2}{5}, \\ 0, & \text{otherwise}. \end{cases} \tag{4.20}$$

and a zero boundary condition $u(\pm 2, t) = 0$ is considered.

The well-performed numerical simulations for capturing the discontinuity in the sharp interface and the accurate transition between the parabolic and hyperbolic regions with different numbers of grid points at $T = 0.7$ are presented in Fig. 13(up left). At the edge of transition regions, a small oscillation can be observed for hybrid DWENO and hybrid MRWENO while hybrid HWENO scheme gives more proper result in Fig. 13(up right). The troubled-cell trace of three hybrid schemes are also plotted in Fig. 13(bottom three).

Table 3 The comparison of errors and rates of convergence of different numerical schemes at $T = 2$ in interval $x \in [-\pi, \pi]$ for Example 6

	Hybrid HWENO		Hybrid DWENO		Hybrid MRWENO	
N	L_∞	Order	L_∞	Order	L_∞	Order
10*10	2.2438e–05		2.5362e–06		5.6064e–06	
20*20	1.0469e–06	4.4217	6.3004e–08	5.3311	6.9399e–08	6.3360
40*40	3.7137e–08	4.8171	9.9345e–10	5.9869	9.9828e–10	6.1193
80*40	1.2018e–09	4.9496	1.5265e–11	6.0241	1.5267e–11	6.0310
N	L_1	Order	L_1	Order	L_1	Order
10*10	1.2002e–05		1.6772e–06		3.5985e–06	
20*20	6.0417e–07	4.3121	3.9858e–08	5.3950	4.3718e–08	6.3631
40*40	2.2528e–08	4.7451	6.3078e–10	5.9816	6.3384e–10	6.1080
80*80	7.4661e–10	4.9152	9.7117e–12	6.0213	9.7127e–12	6.0281
N	L_2	Order	L_2	Order	L_2	Order
10*10	1.4461e–05		1.9201e–06		4.1511e–06	
20*20	7.0586e–07	4.3566	4.4648e–08	5.4265	4.9017e–08	6.4041
40*40	2.5641e–08	4.7829	7.0227e–10	5.9904	7.0568e–10	6.1181
80*80	8.3954e–10	4.9327	1.0793e–11	6.0238	1.0794e–11	6.0306

Example 6 Considering the two-dimensional diffusion equation to observe the accuracy:

$$u_t = u_{xx} + u_{yy}, \quad -\pi \le x \le \pi, -\pi \le y \le \pi. \tag{4.21}$$

The initial condition is taken as $u(x, y, 0) = \sin(x + y)$ with periodic boundary condition. The exact solution is $u(x, y, t) = e^{-2t} \sin(x + y)$.

Tables 3 and 4 show the errors and rate of convergency in terms of L_1, L_2 and L_∞ norms at $T = 2$ in $x \in [-\pi, \pi]$ and CPU time of hybrid DWENO, hybrid MRWENO schemes and present scheme, respectively. Since the problem is smooth, there is no troubled-cells to be marked, and also the modification of the first-order moment for our scheme. On the other hand, our reconstruction is based on fifth-order finite volume HWENO mythology [49] in the least square sense while the other two schemes is based on dimension-by-dimension manner. Therefore, fifth-order convergency can be achieved for this two-dimensional smooth problem. However, if the solution is discontinuous, then present scheme gives fourth-order accurate computational result for two-dimensional tests in general. It is well known, for two or higher dimension cases, the finite difference schemes will cost less CPU time than finite volume schemes with same rectangular meshes. From Table 4 we can see that hybrid HWENO costs more CPU time than Hybrid DWENO, Hybrid MRWENO in test case.

Example 7 Considering the two-dimensional PME equation:

$$u_t = (u^2)_{xx} + (u^2)_{yy}, \quad -10 \le x \le 10, -10 \le y \le 10. \tag{4.22}$$

Table 4 CPU time of different numerical schemes for Example 6

$N * N$	Hybrid HWENO	Hybrid DWENO	Hybrid MRWENO
10*10	2.0041e+01	1.2969e+00	1.4694e+00
20*20	3.0302e+02	6.8648e+00	9.5529e+00
40*40	4.4157e+03	6.6889e+01	6.8893e+01
80*80	7.0611e+04	6.3636e+02	7.0025e+02

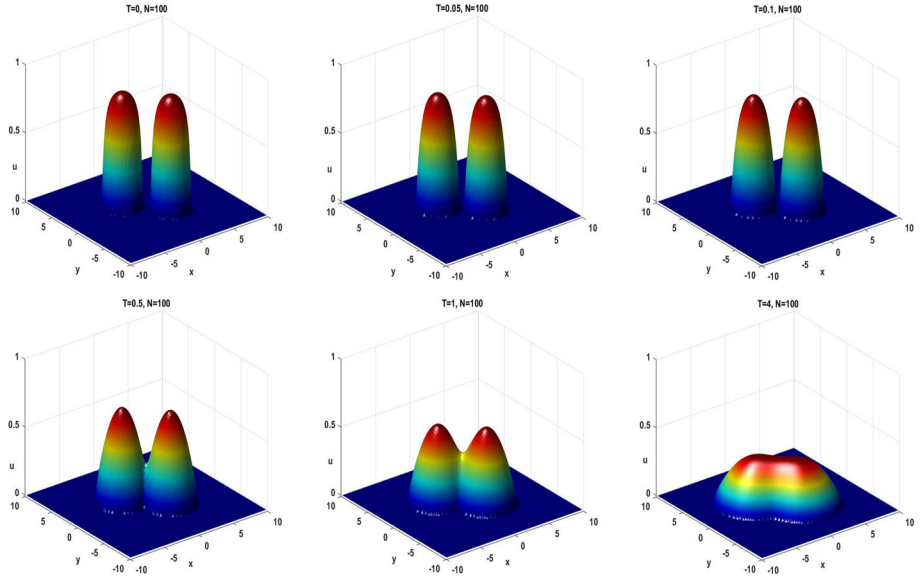

Fig. 14 Numerical solution of hybrid HWENO scheme for two-dimensional PME equation with $N = 100$ of Example 7 at time $T = 0, 0.05, 0.1, 0.5, 1, 4$

with initial data

$$u(x, y, 0) = \begin{cases} e^{\frac{1}{x^2+y^2+4x-4y+2}}, & x^2 + y^2 + 4x - 4y + 2 < 0, \\ e^{\frac{1}{x^2+y^2-4x+4y+2}}, & x^2 + y^2 - 4x + 4y + 2 < 0, \\ 0, & \text{otherwise.} \end{cases} \tag{4.23}$$

The periodic boundary condition is considered for this example. The computation is performed at time $T = 0, 0.05, 0.1, 0.5, 1, 4$. As we can see from Fig. 14, the results indicate that the scheme capable of capturing the sharp interface without spurious oscillation while not marking any troubled-cell, and agree with other related references [24, 32]. In Fig. 15, we also plotted the numerical comparison of hybrid DWENO, hybrid MRWENO and hybrid HWENO scheme in x- and y-direction at time level $T = 0.05$. The numerical superiority of the hybrid HWENO scheme can be observed in both directions.

Example 8 Considering the two-dimensional Buckley–Leverett equation:

$$u_t + \big(F_1(u)\big)_x + \big(F_2(u)\big)_y = \varepsilon\big(u_{xx} + u_{yy}\big), \quad -1.5 \le x \le 1.5, -1.5 \le y \le 1.5. \tag{4.24}$$

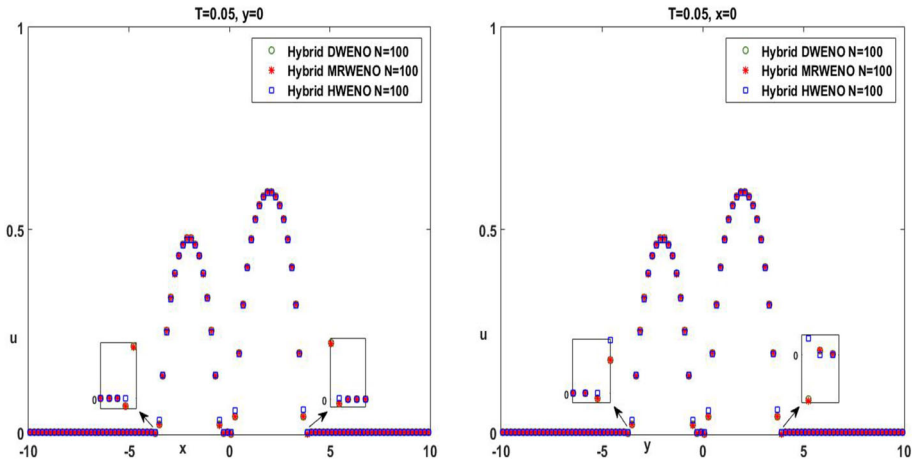

Fig. 15 Numerical solution comparison on x-direction(left) and y-direction(right) of hybrid DWENO, hybrid MRWENO and hybrid HWENO scheme for two-dimensional PME equation with $N = 100$ for Example 7 at time $T = 0.05$

with the flux functions

$$F_1(u) = \frac{u^2}{2u^2 - 2u + 1}, \quad F_2(u) = \frac{u^2}{2u^2 - 2u + 1}\left(-5u^2 + 10u - 4\right). \tag{4.25}$$

We consider periodic boundary conditions in each direction with initial data

$$u(x, y, 0) = \begin{cases} 1, & 2x^2 + 2y^2 < 1, \\ 0, & \text{otherwise.} \end{cases} \tag{4.26}$$

where $\varepsilon = 0.01$.

To demonstrate the efficiency of the numerical scheme for solving this challenging two-dimensional test, we plot the numerical solution(up) and corresponding troubled-cell trajectory(bottom) in Fig. 16 at the time $T = 0, 0.25, 0.5$. The numerical comparison of Hybrid DWENO, Hybrid MRWENO and Hybrid HWENO in x- and y-direction at $T = 0.25$ are also given in Fig. 17(left two), while the troubled-cell traces are provided for hybrid DWENO and MRWENO scheme In Fig. 17(right two).

Example 9 Considering the two-dimensional strongly degenerate parabolic advection-diffusion equation as for the last example:

$$\begin{aligned} u_t + \left(F_1(u)\right)_x + \left(F(u)_2\right)_y = \varepsilon\left(\left(v(u)u_x\right)_x + \left(v(u)u_y\right)_y\right), \quad -1.5 \\ \leq x \leq 1.5, -1.5 \leq y \leq 1.5. \end{aligned} \tag{4.27}$$

with the initial data

$$u(x, y, 0) = \begin{cases} -1, & (2x - 1)^2 + (2y - 1)^2 < 0.64, \\ 1, & (2x + 1)^2 + (2y + 1)^2 < 0.64, \\ 0, & \text{otherwise.} \end{cases} \tag{4.28}$$

and zero boundary condition for each direction, where $\varepsilon = 0.1$, $F_1(u) = F_2(u) = u^2$ and $v(u)$ is the same one in example 5.

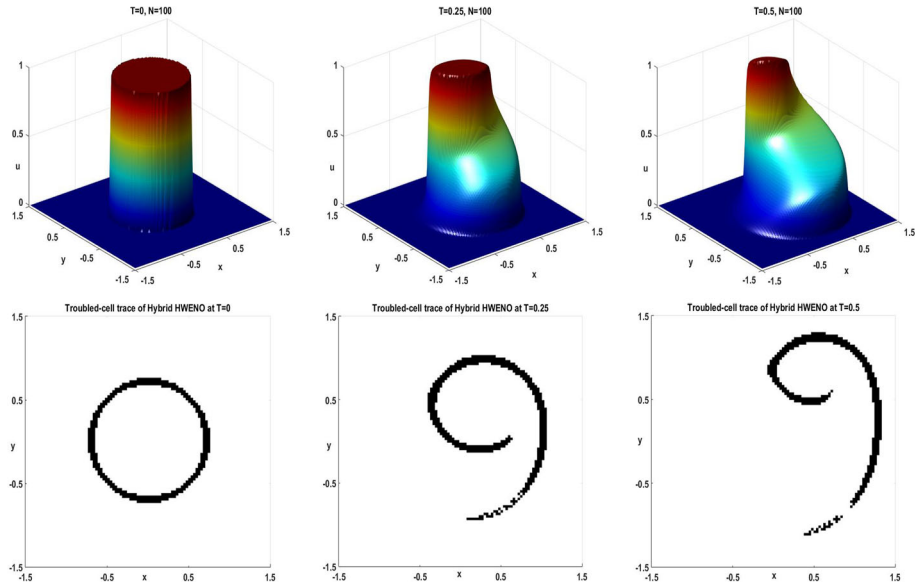

Fig. 16 Numerical solution of two-dimensional Buckley–Leverett equation at $T = 0, 0.25, 0.5$ with $N = 100$ for Example 8(up) and troubled-cell trace(bottom)

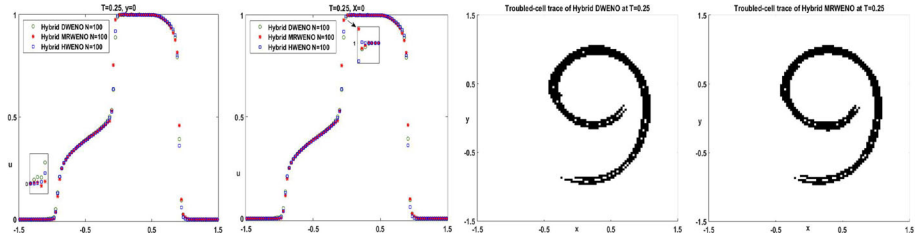

Fig. 17 Numerical comparison of Hybrid DWENO, Hybrid MRWENO and Hybrid HWENO scheme in x- and y-direction(left two)for two-dimensional Buckley–Leverett equation at $T = 0.25$ with $N = 100$ for Example 8 and corresponding troubled-cell trace of DWENO and MRWENO scheme(right two)

Numerical performance without having oscillation at the transition zone of the hyperbolic and parabolic region at time level $T = 0, 0.25, 0.5$ can be seen in Fig. 18(up) along with the troubled-cell trajectory plot in Fig. 18(bottom). In Fig. 19(left two), we also compared the numerical results of Hybrid DWENO, Hybrid MRWENO and Hybrid HWENO in x- and y-direction at $T = 0.25$. The Hybrid HWENO scheme gives better results than other two schemes. Our scheme performed well in eliminating spurious numerical oscillation in the sharp interface. The troubled-cell marks are also given for hybrid DWENO and MRWENO scheme In Fig. 19(right two).

5 Concluding Remark

We derive the fifth-order hybrid HWENO scheme for nonlinear degenerate parabolic equations by approximating the diffusion term with hybrid HWENO scheme assist with DDG

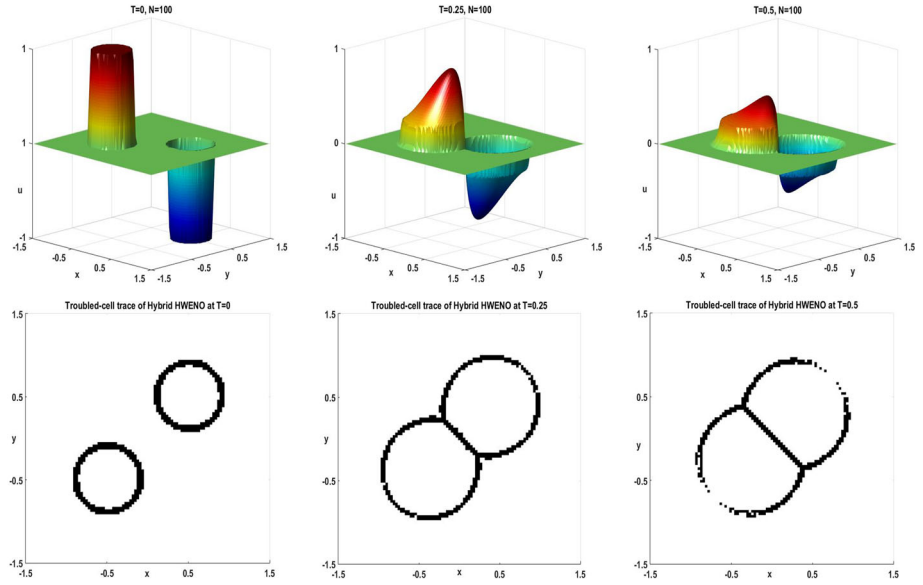

Fig. 18 Numerical solution of Hybrid HWENO scheme for two-dimensional strongly degenerate parabolic convection-diffusion equation at $T = 0, 0.25, 0.5$ with $N = 100$ for Example 9(up) and corresponding troubled-cell trace(bottom)

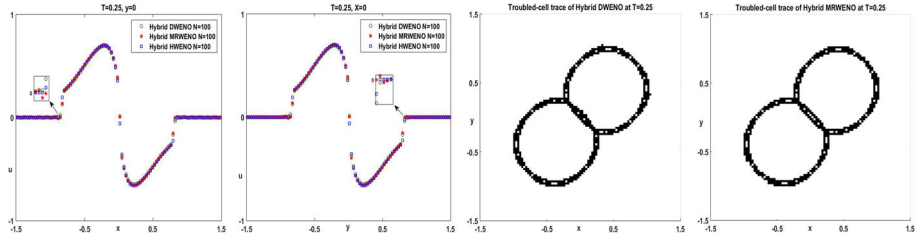

Fig. 19 Numerical comparison of Hybrid DWENO, Hybrid MRWENO and Hybrid HWENO scheme in x- and y-direction(left two)for two-dimensional strongly degenerate parabolic convection-diffusion equation at $T = 0.25$ with $N = 100$ for Example 9n and corresponding troubled-cell trace of DWENO and MRWENO scheme(right two)

flux in this paper. The spatial reconstruction is performed by using the zero- and first-order moments, and the TVD-RK3 method is used in temporal discretization. A trouble-cell indicator is applied to identify the discontinuity and the HWENO reconstruction is applied in these troubled-cells to avoid the oscillation while using straightforward linear approximation in the smooth regions. The present scheme approximates the diffusion term by only using the information in immediate neighbor stencils. Extensive numerical experiments are provided for diffusion-domain equations, such as diffusion equation, PME equation, Buckley–Leverett equation, strongly degenerate parabolic convection-diffusion equation. The hybrid HWENO scheme is effective and has the advantages of high-order computational accuracy and essentially non-oscillatory property for all test cases. It is well known, for two or higher dimension cases, the finite difference schemes will cost less CPU time than finite volume schemes with same rectangular meshes. As a result, hybrid HWENO costs more CPU time than Hybrid DWENO, Hybrid MRWENO in two dimensional test cases. It is well known fact that high

order finite difference WENO scheme can be only constructed on rectangular meshes or the meshes can be mapped into rectangular meshes with high order mapping. On the other hand, finite volume WENO/HWENO schemes have more potential to extend to unstructured grids, such as triangular mesh, which is our next work.

Data Availablity Data sharing not applicable to this article as no datasets were generated or analyzed during the current study.

Declarations

Conflict of interest The authors declare that we have no conflict of interest.

References

1. Abedian, R.: A new high-order weighted essentially non-oscillatory scheme for non-linear degenerate parabolic equations. Numer. Methods Partial Differ. Equ. **37**(2), 1317–1343 (2021)
2. Abedian, R., Adibi, H., Dehghan, M.: A high-order weighted essentially non-oscillatory (WENO) finite difference scheme for nonlinear degenerate parabolic equations. Comput. Phys. Commun. **184**(8), 1874–1888 (2013)
3. Abedian, R., Dehghan, M.: A high-order weighted essentially nonoscillatory scheme based on exponential polynomials for nonlinear degenerate parabolic equations. Numer. Methods Part. Differ. Equ. **38**(4), 970–996 (2022)
4. Alt, H.W., Luckhaus, S.: Quasilinear elliptic-parabolic differential equations. Math. Z. **183**(3), 311–341 (1983)
5. Arbogast, T., Huang, C.-S., Zhao, X.: Finite volume WENO schemes for nonlinear parabolic problems with degenerate diffusion on non-uniform meshes. J. Comput. Phys. **399**, 108921 (2019)
6. Aregba-Driollet, D., Natalini, R., Tang, S.: Explicit diffusive kinetic schemes for nonlinear degenerate parabolic systems. Math. Comput. **73**(245), 63–94 (2004)
7. Aronson, D.G.: The porous medium equation. In: Nonlinear Diffusion Problems, pp. 1–46. Springer (1986)
8. Balsara, D.S., Shu, C.-W.: Monotonicity preserving weighted essentially non-oscillatory schemes with increasingly high order of accuracy. J. Comput. Phys. **160**(2), 405–452 (2000)
9. Bendahmane, M., Bürger, R., Ruiz-Baier, R., Schneider, K.: Adaptive multiresolution schemes with local time stepping for two-dimensional degenerate reaction-diffusion systems. Appl. Numer. Math. **59**(7), 1668–1692 (2009)
10. Bessemoulin-Chatard, M., Filbet, F.: A finite volume scheme for nonlinear degenerate parabolic equations. SIAM J. Sci. Comput. **34**(5), B559–B583 (2012)
11. Borges, R., Carmona, M., Costa, B., Don, W.S.: An improved weighted essentially non-oscillatory scheme for hyperbolic conservation laws. J. Comput. Phys. **227**(6), 3191–3211 (2008)
12. Burbeau, A., Sagaut, P., Bruneau, C.-H.: A problem-independent limiter for high-order Runge–Kutta discontinuous Galerkin methods. J. Comput. Phys. **169**(1), 111–150 (2001)
13. Cai, X., Zhang, X., Qiu, J.: Positivity-preserving high order finite volume HWENO schemes for compressible Euler equations. J. Sci. Comput. **68**(2), 464–483 (2016)
14. Castro, M., Costa, B., Don, W.S.: High order weighted essentially non-oscillatory WENO-Z schemes for hyperbolic conservation laws. J. Comput. Phys. **230**(5), 1766–1792 (2011)
15. Cavalli, F., Naldi, G., Puppo, G., Semplice, M.: High-order relaxation schemes for nonlinear degenerate diffusion problems. SIAM J. Numer. Anal. **45**(5), 2098–2119 (2007)
16. Cockburn, B., Shu, C.-W.: TVB Runge–Kutta local projection discontinuous Galerkin finite element method for conservation laws. II. General framework. Math. Comput. **52**(186), 411–435 (1989)
17. Ghosh, D., Dorf, M.A., Dorr, M.R., Hittinger, J.A.F.: Kinetic simulation of collisional magnetized plasmas with semi-implicit time integration. J. Sci. Comput. **77**(2), 819–849 (2018)
18. Gottlieb, S., Ketcheson, D.I., Shu, C.-W. Strong Stability Preserving Runge–Kutta and Multistep Time Discretizations. World Scientific (2011)
19. Hajipour, M., Malek, A.: High accurate NRK and MWENO scheme for nonlinear degenerate parabolic PDEs. Appl. Math. Model. **36**(9), 4439–4451 (2012)
20. Henrick, A.K., Aslam, T.D., Powers, J.M.: Mapped weighted essentially non-oscillatory schemes: achieving optimal order near critical points. J. Comput. Phys. **207**(2), 542–567 (2005)

21. Changqing, H., Shu, C.-W.: Weighted essentially non-oscillatory schemes on triangular meshes. J. Comput. Phys. **150**(1), 97–127 (1999)
22. Hu, X.Y., Wang, Q., Adams, N.A.: An adaptive central-upwind weighted essentially non-oscillatory scheme. J. Comput. Phys. **229**(23), 8952–8965 (2010)
23. Jiang, G.-S., Shu, C.-W.: Efficient implementation of weighted ENO schemes. J. Comput. Phys. **126**(1), 202–228 (1996)
24. Jiang, Y.: High order finite difference multi-resolution WENO method for nonlinear degenerate parabolic equations. J. Sci. Comput. **86**(1), 1–20 (2021)
25. Johnson, C.: Adaptive finite element methods for conservation laws. In: Advanced Numerical Approximation of Nonlinear Hyperbolic Equations, pp. 269–323. Springer (1998)
26. Kong, R., Spanier, J.: Transport-constrained extensions of collision and track length estimators for solutions of radiative transport problems. J. Comput. Phys. **242**, 682–695 (2013)
27. Krivodonova, L., Xin, J., Remacle, J.-F., Chevaugeon, N., Flaherty, J.E.: Shock detection and limiting with discontinuous Galerkin methods for hyperbolic conservation laws. Appl. Numer. Math. **48**(3–4), 323–338 (2004)
28. Levy, D., Puppo, G., Russo, G.: Compact central WENO schemes for multidimensional conservation laws. SIAM J. Sci. Comput. **22**(2), 656–672 (2000)
29. Liu, H., Yan, J.: The direct discontinuous Galerkin (DDG) methods for diffusion problems. SIAM J. Numer. Anal. **47**(1), 675–698 (2009)
30. Liu, H., Qiu, J.: Finite difference Hermite WENO schemes for conservation laws, II: an alternative approach. J. Sci. Comput. **66**(2), 598–624 (2016)
31. Liu, X.-D., Osher, S., Chan, T.: Weighted essentially non-oscillatory schemes. J. Comput. Phys. **115**(1), 200–212 (1994)
32. Liu, Y., Shu, C.-W., Zhang, M.: High order finite difference WENO schemes for nonlinear degenerate parabolic equations. SIAM J. Sci. Comput. **33**(2), 939–965 (2011)
33. Muskat, M.: The flow of homogeneous fluids through porous media. Soil Sci. **46**(2), 169 (1938)
34. Otto, F.: L1-contraction and uniqueness for quasilinear elliptic-parabolic equations. J. Differ. Equ. **131**(1), 20–38 (1996)
35. Pomraning, G.C., Foglesong, G.M.: Transport-diffusion interfaces in radiative transfer. J. Comput. Phys. **32**(3), 420–436 (1979)
36. Qiu, J., Shu, C.-W.: Hermite WENO schemes and their application as limiters for Runge–Kutta discontinuous Galerkin method: one-dimensional case. J. Comput. Phys. **193**(1), 115–135 (2004)
37. Qiu, J., Shu, C.-W.: A comparison of troubled-cell indicators for Runge–Kutta discontinuous Galerkin methods using weighted essentially nonoscillatory limiters. SIAM J. Sci. Comput. **27**(3), 995–1013 (2005)
38. Qiu, J., Shu, C.-W.: Hermite WENO schemes and their application as limiters for Runge–Kutta discontinuous Galerkin method II: Two dimensional case. Comput. Fluids **34**(6), 642–663 (2005)
39. Radu, F.A., Pop, I.S., Knabner, P.: Error estimates for a mixed finite element discretization of some degenerate parabolic equations. Numerische Mathematik **109**(2), 285–311 (2008)
40. Rathan, S., Kumar, R., Jagtap, A.D.: L1-type smoothness indicators based WENO scheme for nonlinear degenerate parabolic equations. Appl. Math. Comput. **375**, 125112 (2020)
41. Rider, W.J., Margolin, L.G.: Simple modifications of monotonicity-preserving limiter. J. Comput. Phys. **174**(1), 473–488 (2001)
42. Shu, C.-W.: Essentially non-oscillatory and weighted essentially non-oscillatory schemes for hyperbolic conservation laws. In: Advanced Numerical Approximation of Nonlinear Hyperbolic Equations, pp. 325–432. Springer (1998)
43. Suresh, A., Huynh, H.T.: Accurate monotonicity-preserving schemes with Runge–Kutta time stepping. J. Comput. Phys. **136**(1), 83–99 (1997)
44. Tao, Z., Li, F., Qiu, J.: High-order central Hermite WENO schemes: dimension-by-dimension moment-based reconstructions. J. Comput. Phys. **318**, 222–251 (2016)
45. Van Duyn, C.J., Peletier, L.A.: Nonstationary filtration in partially saturated porous media. Arch. Ration. Mech. Anal. **78**(2), 173–198 (1982)
46. Vázquez, J.L.: The Porous Medium Equation: Mathematical Theory. Oxford University Press on Demand (2007)
47. Zahran, Y.H., Abdalla, A.H.: Seventh order Hermite WENO scheme for hyperbolic conservation laws. Comput. Fluids **131**, 66–80 (2016)
48. Zhang, Q., Zi-Long, W.: Numerical simulation for porous medium equation by local discontinuous Galerkin finite element method. J. Sci. Comput. **38**(2), 127–148 (2009)
49. Zhao, Z., Qiu, J.: A Hermite WENO scheme with artificial linear weights for hyperbolic conservation laws. J. Comput. Phys. **417**, 109583 (2020)

50. Zheng, N., Cai, X., Qiu, J.-M., Qiu, J.: A conservative semi-Lagrangian hybrid hermite WENO scheme for linear transport equations and the nonlinear Vlasov–Poisson system. SIAM J. Sci. Comput. **43**(5), A3580–A3606 (2021)
51. Zhu, J., Qiu, J.X.: A class of the fourth order finite volume Hermite weighted essentially non-oscillatory schemes. Sci. China Ser. A Math. **51**(8), 1549–1560 (2008)
52. Zhu, J., Qiu, J.: A new fifth order finite difference WENO scheme for solving hyperbolic conservation laws. J. Comput. Phys. **318**, 110–121 (2016)
53. Zhu, J., Shu, C.-W.: A new type of multi-resolution WENO schemes with increasingly higher order of accuracy. J. Comput. Phys. **375**, 659–683 (2018)